scientific reports

Check for updates

OPEN

Engineering the coordination environment of Ni and Pd dual active sites for promoting the oxygen reduction reaction

Lei Li[1,2]✉, Xiaoxia Wu[1,2], Ruotong Zhang[1,2], Narsu Bai[1,2], Min Zhang[1,2] & Yuhua Wen[3]✉

Precisely regulating active sites is vital for promoting the oxygen reduction reaction (ORR) activity. Here we reported highly active Ni-Pd co-doped N-coordinated graphene towards ORR achieved by edge termination and O doping. Our first-principles calculations demonstrated that edge termination effectively boost the ORR activity, and armchair-edge termination was energetically more favorable than zigzag-edge termination. Notably, after O doping Ni-Pd active center, armchair edge-terminated Ni-Pd active site exhibited better ORR activity, and the lowest overpotential was only 0.31 V. This improvement in activity was attributed to the shift of the *d*-band center of Ni atom toward the Fermi-level and the shift of the *d*-band center of Pd atom away from the Fermi-level, thus regulating the *OH adsorption strength. This work paves the way for developing highly active graphene-based dual-atom catalysts for ORR through edge and doping engineering.

Keywords Oxygen reduction reaction, Graphene, Edge termination, O doping, Density-functional theory

The exploration of clean and renewable energy materials as well as their devices becomes an urgent demand when being confronted with the energy crisis and environmental problems[1,2]. Owing to high energy density and environmental friendliness, metal-air batteries and fuel cells have been become promising candidates for energy storage devices[2–4]. The slow oxygen reduction reaction (ORR) kinetics at the cathode, however, severely impedes their practical applications. Despite excellent ORR kinetic activity of Pt catalysts, the rare reserve and high cost heavily limit their practical use[5,6]. Therefore, developing high-efficiency, low-cost, and well durable alternatives to Pt catalysts still remains a persistent challenge for electrocatalysis.

Recently, dual-atom catalysts (DACs), especially N-doped graphene-based dual transition metal atoms systems (denoted as M_1M_2-N-Gs), have shown great application prospects[7–11]. Since the coordination structure of active site determines the catalytic activity[11–15], more efforts focus on the improvement of the catalytic performances of M_1M_2-N-Gs through changing the local environment of active site. It is known that dispersing the active site at graphene edge is a potent approach for boosting the catalytic activity of graphene-based catalysts towards various chemical reactions. For example, the defective NiN_3 active site at the edge achieved a carbon dioxide reduction reaction (CO_2RR) performance and durability superior to the interior NiN_3 active site[16]. Atomically dispersed FeN_4 active sites near graphitic edges also exhibited higher ORR activity and durability compared with commercial Pt/C catalyst[17–19]. Density-functional theory (DFT) calculations further verified that the enhanced ORR activity originates from tilted-FeN_4 configurations at edges[20]. The edges with vacancy defects lowered the energy barrier of ORR on $CoZnN_6$- and $FeCoN_6$-Gs, thus enhancing their catalytic activities[21–23]. Besides widely investigated Fe- and Co-based DACs[11,24], $NiNiN_6$-G[25], $NiCuN_6$-G[26], and $NiZnN_6$-G[27] were screened out by combining DFT calculations and machine learning techniques, demonstrating their good ORR catalytic activities. Pd, as a congener element of Ni, is expected to have a synergistic effect with Ni atom, thus achieving the suitable electronic structures to adsorb ORR intermediates. Moreover, Ni-Pd nanoparticles impregnated on nitrogen-doped graphene and reduced graphene oxide graphene have been confirmed to have outstanding ORR catalytic performances[28–30]. Therefore, despite the unsatisfactory catalytic activities of NiN_4 and PdN_4 embedded graphenes[31–33], $NiPdN_6$-G may possess good activity for ORR and their catalytic performance could be further enhanced by edge terminal engineering. Furthermore, due to the multiple possibilities of coordination

[1]College of Physics and Electronic Information, Inner Mongolia Normal University, Hohhot 010022, China. [2]Inner Mongolia Key Laboratory for Physics and Chemistry of Functional Materials, Hohhot 010022, China. [3]Department of Physics, Xiamen University, Xiamen 361005, China. ✉email: lilei@imnu.edu.cn; yhwen@xmu.edu.cn

structures of edge terminated $NiPdN_6$-G, there still lacks a fundamental understanding on how the structure of edge termination affects the catalytic activity.

Additionally, O doping may modulate the electronic structures of active sites and promote the ORR activity. For example, DFT calculations demonstrated that O-doped graphene supported Pt catalyst has excellent ORR catalytic activity among a series of B, N, and O doped structures[34]. O and N co-coordination can induce the shifts in the *d*-band center of Mo atom towards the Fermi-level, resulting in the prominent ORR activity of MoN_2O_2-G[35]. Recently, synthesized $FeCuN_4O_2$-G and $FeCuN_5O$-G presented remarkably lowered activation energy and enhanced intrinsic ORR activity compared with $FeCuN_6$-G[12,36,37]. Nevertheless, whether O doping at edge-terminated $NiPdN_6$-G can further improve their catalytic performance towards ORR remains unknown. Hence, there is an urgent demand to comprehensively explore the modulation of ORR activity for $NiPdN_6$-G through edge termination and O dopant.

Herein, in this work we performed DFT calculations to thoroughly investigate the electrochemical activity of $NiPdN_6$-G with and without edge termination and O doping. Our results show that edge termination and O doping can effectively promote the catalytic activity for ORR, and the lowest overpotential is only 0.31 V. This work provides a theoretical guidance for rational design of low-cost and high-efficiency graphene-based DACs.

Computational method

We performed the spin-polarized DFT calculations with the Vienna ab initio simulation package (VASP)[38,39]. The Perdew-Burke-Ernzerhof (PBE) functional method within the generalized gradient approximation (GGA) was used to treat electronic exchange–correlation interactions[40]. $M_1M_2N_6$ respectively located in the interior and edge sites of graphene were constructed by using 6×6 graphene supercell containing 72 C atoms and graphene nanoribbon containing 72 C and 12 H atoms (see Fig. S1), respectively. The kinetic energy cutoff was set as 500 eV to keep the energy convergence. All structures were allowed to relax until the electronic structure iteration and atomic force were respectively smaller than 10^{-5} eV and 0.02 eV/Å. The sufficient vacuums of 15 Å in the *c* direction for interior Ni-Pd catalyst and about 15 Å in the *b* direction for edge-hosted Ni-Pd catalysts were used to avoid the interactions between the models and their mirror images. The k-meshes of $3\times3\times1$ and $3\times1\times1$ were used for the structural optimizations of interior and edge-hosted structures, respectively. The van der Waals interactions between catalysts and reaction intermediates were described using the DFT + D3 dispersion correction method[41].

The formation energy (E_f) of all catalysts was calculated according to the equation as follow

$$E_f = E_t - E_{Ni} - E_{Pd} - n\mu_X, \tag{1}$$

where E_t, E_{Ni}, and E_{Pd} are the energies of catalysts, isolated Ni and Pd atoms, respectively. μ_X represents the chemical potentials of C, N, O, or H atom, which is defined as the energy of C atom in perfect graphene, N atom in N_2 molecule, O atom in O_2 molecule, or H atom in H_2 molecule, respectively. *n* denotes the numbers of C, N, O, or H atoms.

The adsorption energy (E_{ads}) of reaction intermediate on catalyst was defined as

$$E_{ads} = E_{catal+inter} - E_{inter} - E_{catal}, \tag{2}$$

where $E_{catal+inter}$, E_{catal}, and E_{inter} respectively represent the energies of catalyst with adsorbed reaction intermediate, catalyst, and isolated reaction intermediate.

The free energy change (ΔG) of each reaction step was obtained according to the equation as follow

$$\Delta G = \Delta E + \Delta ZPE - T\Delta S + \Delta G_U + \Delta G_{pH}, \tag{3}$$

where ΔE, ΔZPE, and ΔS correspond to the changes in total energy, zero-point energy, and entropy of each reaction step, respectively. *T* is set to be 298.15 K, corresponding to the room temperature. $\Delta G_U = -meU$, in which *m* denotes the number of electrons transferred during the reaction process, and *U* denotes the electrode potential. ΔG_{pH} is equal to $k_BT\times\ln10\times pH$, where k_B is the Boltzmann constant, and pH is set to be 0 in an acidic medium.

For $O_2 \rightarrow {}^*OOH \rightarrow {}^*O + H_2O \rightarrow {}^*OH + H_2O \rightarrow 2H_2O$ along the four-electron reaction pathway, the free energy change (ΔG) for each reaction step was respectively calculated according to the equations as follows

$$\Delta G_1 = \Delta G_{*OOH} - 4.92 + eU, \tag{4}$$

$$\Delta G_2 = \Delta G_{*O} - \Delta G_{*OOH} + eU, \tag{5}$$

$$\Delta G_3 = \Delta G_{*OH} - \Delta G_{*O} + eU, \tag{6}$$

$$\Delta G_4 = -\Delta G_{*OH} + eU. \tag{7}$$

Finally, the overpotential (η) was obtained by the following equation

$$\eta = 1.23 + \max(\Delta G_1, \Delta G_2, \Delta G_3, \Delta G_4)/e. \tag{8}$$

Results and discussion

Integrating N_6-coordinated M_1-M_2 active site into the interior, zigzag-edge and armchair-edge of graphene can form one interior ($M_1M_2N_6$-I), six zigzag-edge ($M_1M_2N_6$-A1 ~ A6), and four armchair-edge ($M_1M_2N_6$-Z1 ~ Z4) configurations, as shown in Fig. 1. However, due to the differences in the local N coordination environments

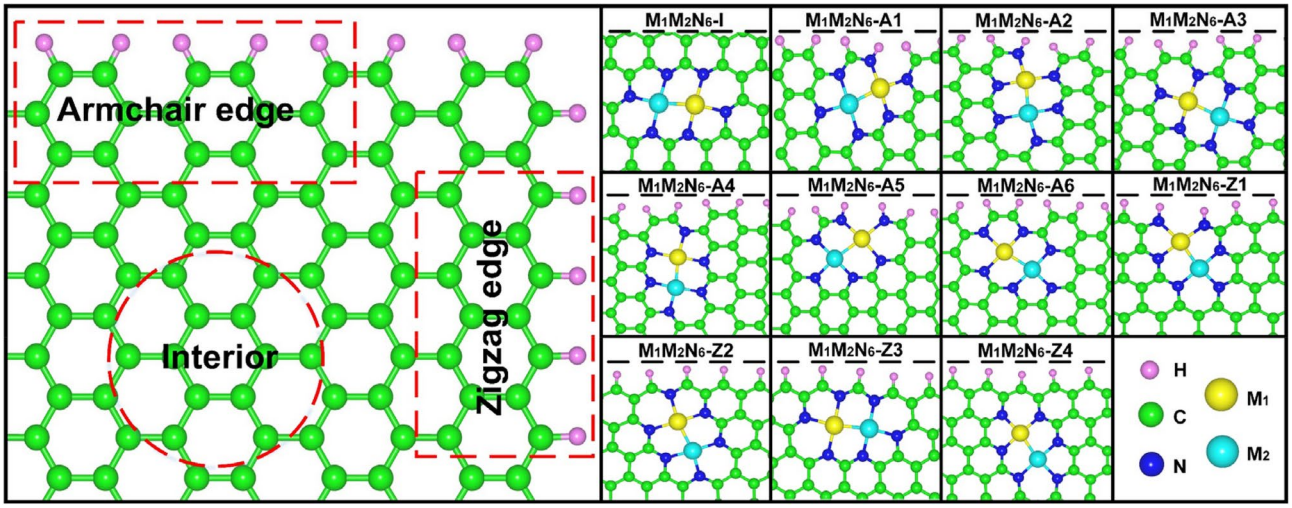

Fig. 1. Schematic diagram of $M_1M_2N_6$ located in the interior (-I), armchair-edge (– A1 ~ A6), and zigzag-edge (– Z1 ~ Z4) of graphene. The pink, green, blue, yellow, and balls denote H, C, N, M_1, and M_2 atoms, respectively.

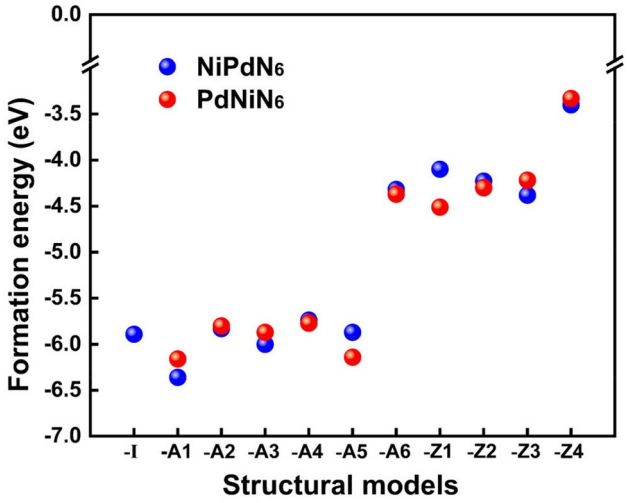

Fig. 2. The formation energy of $M_1M_2N_6$ with different active sites.

of M_1 and M_2 atoms located in the edge, the exchange of both atoms can form different active site. Therefore, there exist twenty-one possible Ni-Pd co-doped N_6-coordinated graphene structures in total, namely $NiPdN_6$-I, $NiPdN_6$-A1 ~ A6, $PdNiN_6$-A1 ~ A6, $NiPdN_6$-Z1 ~ Z4, and $PdNiN_6$-Z1 ~ Z4. To identify their thermodynamic stability, the formation energy (E_f) was illustrated in Fig. 2 and Table S1. One can find that for all structures, the E_f are negative, implying that they are structurally stable and plausible to exist on the graphene. It is noted that, except $NiPdN_6$-A6 and $PdNiN_6$-A6 configurations, other $NiPdN_6$ and $PdNiN_6$ structures in armchair-edge have smaller E_f than those in zigzag-edge, so the probability of these structures in armchair-edge should be higher than that in zigzag-edge. Moreover, the E_f of these structures in armchair-edge were close to or less than that of the standard $NiPdN_6$-I structure, suggesting that the $NiPdN_6$ and $PdNiN_6$ structures may be prone to be formed in the armchair-edge. In addition, the exchange of Ni and Pd atoms led to certain differences of E_f (0.02 ~ 0.41 eV) for each edge structure. Among which, the energy differences between $NiPdN_6$-A2/A4/A6/Z2/Z4 and $PdNiN_6$-A2/A4/A6/Z2/Z4 are smaller than 0.1 eV, while $NiPdN_6$-A1/A3/Z3 and $PdNiN_6$-A5/Z1 have markedly smaller E_f than that of $PdNiN_6$-A1/A3/Z3 and $NiPdN_6$-A5/Z1. Therefore, except $PdNiN_6$-A1/A3/Z3 and $NiPdN_6$-A5/Z1, all the $NiPdN_6$ and $PdNiN_6$ structures were considered in the following discussion to identify their ORR catalytic activities.

Since the adsorption of reaction intermediate has a great effect on the ORR catalytic activity, the adsorption characteristics of all ORR intermediates ($*O_2$, *OOH, *O, and *OH) were firstly investigated. By optimizing their adsorptions on all catalysts, the most stable adsorption structures were illustrated in Fig. 3a. One can find that the $*O_2$ and *OOH are only stably adsorbed on Ni atom in all catalysts, while *O and O in *OH may bond

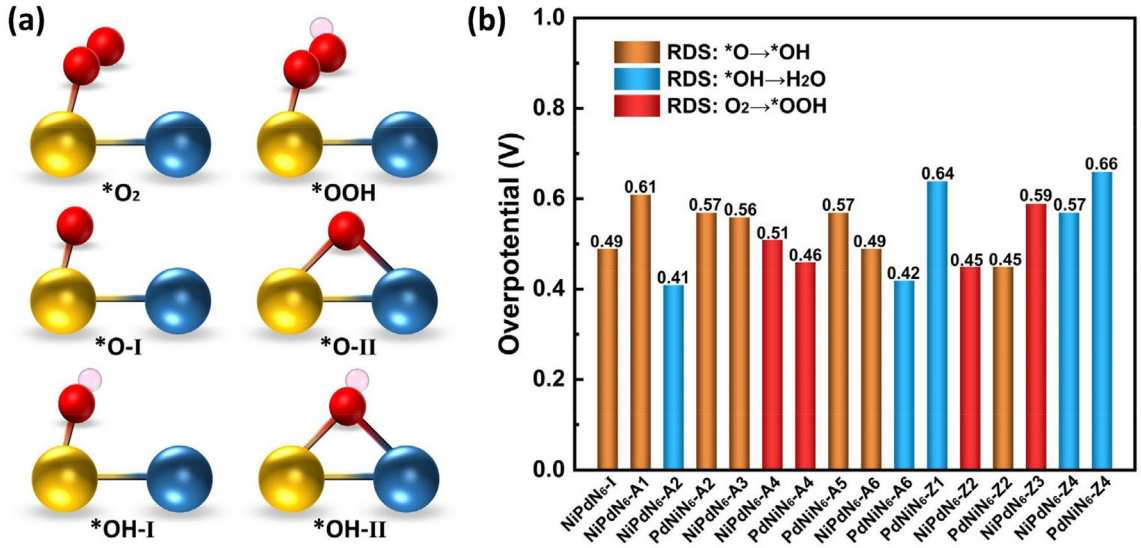

Fig. 3. (**a**) Schematic diagram for the intermediate adsorption structures. (**b**) The overpotentials of ORR on $NiPdN_6$ and $PdNiN_6$ structures. The yellow, blue, red, and pink balls denote Ni, Pd, O, and H atoms, respectively.

with single Ni or both Ni and Pd atoms. Therefore, Ni atom is the main active site for the adsorption of ORR intermediates, which was confirmed by the fact that Ni atom loses more charges than Pd atom in all $NiPdN_6$ and $PdNiN_6$ structures (see Table S2). Considering that the adsorption strength to reactants directly affects the activity of catalysts, E_{ads} for these intermediates were further calculated by Eq. (2) and listed in Table S3. By comparison with $NiPdN_6$-I, the E_{ads} for all intermediates were changed at the edge active sites to different extent. According to available studies, M_1M_2-N-Gs with the E_{ads} for O_2 in the range of − 0.24 to − 0.80 eV may possess good ORR activity[25,42–46]. Evidently, all E_{ads} of $NiPdN_6$ and $PdNiN_6$ for O_2 in this work (− 0.38 ~ − 0.72 eV) fall in the above range, thus some excellent ORR catalysts are likely to exist in these structures.

To identify the ORR activity of all $NiPdN_6$ structures, the free energy change for each reaction step, the free energy diagram, and the overpotential were calculated by Eqs. (3)–(8), as shown in Table S3 and Figs. S2 and 3b. For $NiPdN_6$-I, the rate-determining step (RDS) of ORR is the hydrogenation of *O to *OH, and the corresponding overpotential is 0.49 V. This value is slightly higher than those in Pt (111) (0.44 V)[47] and Pt (100) (0.47 V)[48], indicating the relatively lower ORR catalytic activity of $NiPdN_6$-I than Pt catalyst. After introducing the edge active sites, the RDS of ORR was transformed into the formation of the second H_2O molecule for $NiPdN_6$-A2, $PdNiN_6$-A6, $PdNiN_6$-Z1, $NiPdN_6$-Z4, and $PdNiN_6$-Z4 as well as the hydrogenation of O_2 to *OOH for $NiPdN_6$-A4, $PdNiN_6$-A4, $NiPdN_6$-Z2, and $NiPdN_6$-Z3. The overpotentials of ORR on $NiPdN_6$-A2, $PdNiN_6$-A6, $NiPdN_6$-Z2, $PdNiN_6$-Z2, and $PdNiN_6$-A4 were respectively lowered to 0.41, 0.42, 0.45, 0.45, and 0.46 V. However, the overpotential was increased in different extent for other structures, which should be attributed to the changed E_{ads} for the ORR intermediates at edge active sites, as indicated by Table S3. Therefore, $NiPdN_6$-A2 and $PdNiN_6$-A6 possess excellent ORR catalytic activity superior to Pt catalyst, while the ORR catalytic activity of $PdNiN_6$-A4, $NiPdN_6$-Z2, and $PdNiN_6$-Z2 is comparable to that of Pt catalyst.

Exploring the scaling relationship between the Gibbs adsorption free energy of reaction intermediates is significant for understanding the catalytic characteristics and developing more effective ORR catalysts. As illustrated in Fig. 4a, ΔG_{*OH} and ΔG_{*OOH} for all catalysts show a clear linear scaling relationship ($\Delta G_{*OOH} = 0.74\Delta G_{*OH} + 3.28$ eV, and the square of the correlation coefficient R^2 is 0.93), indicating their strong relationships. However, the correlations between ΔG_{*O} and $\Delta G_{*OH}/\Delta G_{*OOH}$ are not impressive, and the R^2 respectively are 0.84 and 0.74, as shown in Fig. 4b and c. According to the relationships between these intermediates, an approximately classic volcano curve between ΔG_{*OH} and overpotential was presented in Fig. 4d. Overall, as ΔG_{*OH} increases, the overpotential first reduces and subsequently rises. When ΔG_{*OH} increases to 0.94 eV, the overpotential reaches the minimum (0.29 V), corresponding to the optimal ORR catalytic activity. According to the adsorption free energy of reaction intermediates and the identified RDS, all catalysts can be divided into three regimes under this volcano-like trend. There is a strictly linear left boundary of the volcano curve, and the overpotential is purely dictated by the ΔG_{*OH}. The catalysts in this boundary have strong binding strength to *OH. However, the catalyst sites are more scattered on the right boundary. Among which, the RDS of $NiPdN_6$-A4, $PdNiN_6$-A4, $NiPdN_6$-Z2, and $NiPdN_6$-Z3 is the hydrogenation of O_2 to *OOH. Although the hydrogenation of *O to *OH is the RDS of $NiPdN_6$-I, $NiPdN_6$-A3, and $PdNiN_6$-Z2, the differences between ΔG_1 and ΔG_3 for these catalysts are only 0.07, 0.02, and 0.03 eV (see Table S3), respectively. Thus, the catalysts around the right leg are approximately governed by the weak *OOH binding. In addition, $NiPdN_6$-A1, $PdNiN_6$-A2, $PdNiN_6$-A5, and $NiPdN_6$-A6 with the RDS of the hydrogenation of *O to *OH are located in the middle regime of the above two boundaries, corresponding to the adsorption strength to *O. The less-defined nature reflects the weak correlations between ΔG_{*O} and $\Delta G_{*OH}/\Delta G_{*OOH}$. Therefore, although the ΔG_{*OH} of these catalysts are close

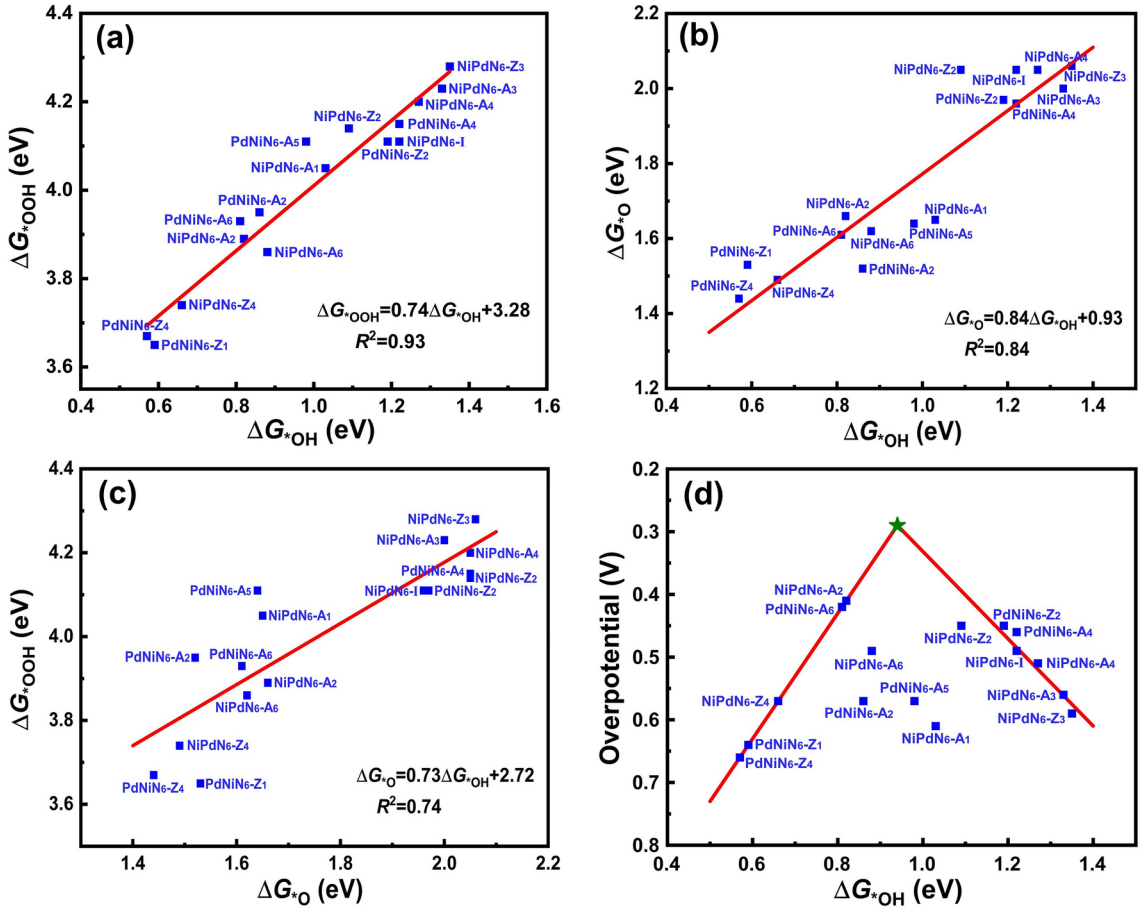

Fig. 4. The scaling relationships for the Gibbs adsorption free energy between (**a**) ΔG_{*OH} and ΔG_{*OOH}, (**b**) ΔG_{*OH} and ΔG_{*O}, and (**c**) ΔG_{*O} and ΔG_{*OOH}. (**d**) The volcano plot of overpotential with ΔG_{*OH}.

to the optimal value of ΔG_{*OH}, their ORR overpotentials are not optimal. In contrast, $NiPdN_6$-A2 with ΔG_{*OH} of 0.82 V is closest to the apex of the volcano plot, thus possesses the best catalytic activity. However, there are still some distances to reach the apex of the volcano plot for this structure. Therefore, it can be inferred that there exists a possibility to further improve the ORR catalytic activity.

Available works have demonstrated a great potential to enhance the ORR catalytic activity of graphene-based metal atom catalysts by doping heterotopic O atom[15,34–37]. Inspired by these works, we try to replace one N atom in $NiPdN_6$-A2 (with the lowest overpotential) with O atom for further enhancing its ORR catalytic activity. In $NiPdN_6$-A2, each N atom can be replaced by O atom (see Fig. 5a), thus there exist six possible Ni-Pd embedded O and N co-coordinated graphene structures (refer to Fig. S3), and the corresponding E_f were calculated by Eq. (1) and illustrated in Fig. 5b. The E_f for these structures are -6.74, -5.77, 7.39, -6.12, -5,75, and -5.64 eV, respectively. In general, the lower value of E_f represents the better structural stability. Therefore, the N1 atom is most likely to be replaced by O atom to form Ni-Pd embedded O and N co-coordinated graphene structure (denoted as $NiPdN_5O$-A2). In addition, it should be noted that 7.39 eV is significantly larger than other values because the $NiPdN_6$-A2 structure undergoes severe deformation after replacing the N3 by O atom (see Fig. S3).

After introducing the O atom into $NiPdN_6$-A2 to form $NiPdN_5O$-A2 structure, the E_{ads} for $*O_2$ was decreased from -0.59 to − 0.61 eV, while the E_{ads} for *OOH, *O, and *OH were increased from − 1.22, − 4.11, and − 2.57 eV to − 0.96, − 3.91, and − 2.39 eV, respectively. Therefore, the ORR catalytic activity of $NiPdN_5O$-A2 may be different from that of $NiPdN_6$-A2. Furthermore, the free energy change and overpotential of ORR on $NiPdN_5O$-A2 were further explored. As displayed in Fig. 6a and Table S3, the downhill free energy for ORR on $NiPdN_5O$-A2 at zero electrode potential (U = 0 V) demonstrates that the ORR process should be exothermic and thermodynamically feasible. With the increasing of electrode potential, $NiPdN_5O$-A2 presents the working potential of 0.94 V during the exothermic reaction process. This value is larger than that (0.82 V) for $NiPdN_6$-A2, indicating that ORR is more prone to proceed on the $NiPdN_5O$-A2. Under the standard ORR potential (U = 1.23 V), the hydrogenation of *O to *OH and the hydrogenation of *OH to H_2O became uphill, indicating these steps are thermodynamically unfavorable. In particular, the maximum free energy barrier of 0.31 eV needs to be overcome in the RDS of the hydrogenation of *OH to H_2O. Hence, the overpotential of ORR on the $NiPdN_5O$-A2 was only 0.31 V. Since the ORR usually takes place in an aqueous electrolyte solution, the solvent effect was evaluated using an implicit solvation model based on the VASPsol[49], and the corresponding free energy diagram was presented in Fig. S4. By comparison with the free change in the gas phase, no remarkable difference in each reaction step was observed.

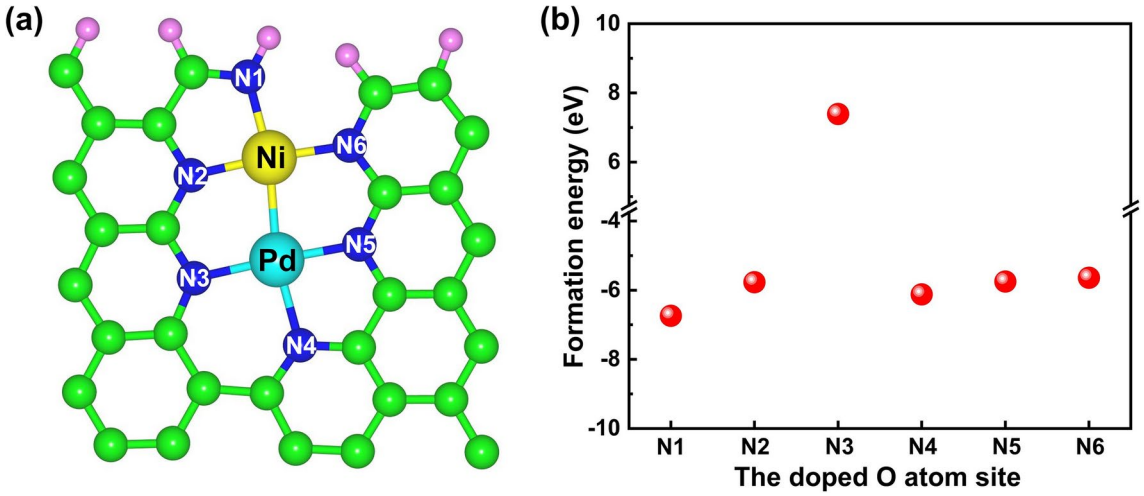

Fig. 5. (**a**) Schematic diagram of the N atom in $NiPdN_6$-A2 that can be replaced by O atom. The pink and green balls denote H and C atoms, respectively. (**b**) Formation energy for the O doped $NiPdN_6$-A2 structure.

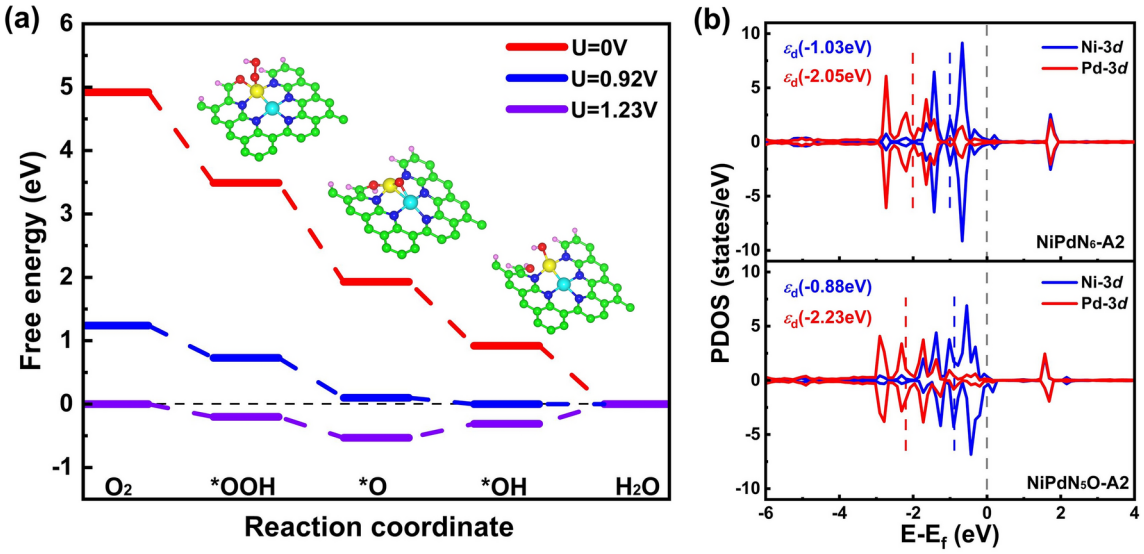

Fig. 6. (**a**) Free energy diagram of ORR on $NiPdN_5O$-A2. (**b**) The PDOS and the *d*-band centers of Ni and Pd atoms in $NiPdN_6$-A2 and $NiPdN_5O$-A2.

The RDS still occurred in the hydrogenation of *OH to H_2O, and the overpotential was slightly increased by 0.06 V, indicating the negligible solvent effect. In comparison to $NiPdN_6$-A2 with larger overpotential (0.41 V), $NiPdN_5O$-A2 should possess higher ORR catalytic activity. Moreover, the overpotential for the $NiPdN_5O$-A2 is remarkably smaller than that for Pt (100) (0.47 V)[47] and Pt (111) (0.44 V)[48], indicating the ORR catalytic activity of the former superior to the latter.

To concretely explore the origin of the superior catalytic activity of $NiPdN_5O$-A2, the projected density of states (PDOS) of *d* orbitals and the *d*-band centers of Ni and Pd atoms in $NiPdN_6$-A2 and $NiPdN_5O$-A2 were calculated, as illustrated in Fig. 6b. One can find that the distribution of *d* orbital and *d*-band center of Ni atom were closer to the Fermi-level than that of Pd atom in $NiPdN_6$-A2, implying that Ni atom should be the main active site for ORR, in agreement with the adsorption structures of intermediates on $NiPdN_6$-A2. When replacing N1 with O atom, the *d* orbital of Ni atom moved towards the Fermi-level, and the *d*-band center were increased from − 1.03 to − 0.88 eV for Ni atom while decreased from − 2.05 to − 2.23 eV for Pd atom. This led to a rising reaction activity of Ni atom and a lowering reaction activity of Pd atom, and the adsorption configuration for *OH was transformed from bonding with Ni and Pd atoms into only binding Ni atom. Eventually, $NiPdN_5O$-A2 presented reduced adsorption capability for *OH (see Table S3) and enhanced ORR catalytic activity.

Conclusions

In summary, our DFT calculations demonstrated that armchair-edge termination was energetically more favorable than zigzag-edge termination. Edge-terminated $NiPdN_6$-Gs, especially armchair edge-terminated $NiPdN_6$-G, presented significantly enhanced ORR catalytic activity as compared with $NiPdN_6$-G without edge termination. After doping O atom into armchair edge-terminated $NiPdN_6$-G, the overpotential was further lowered to 0.31 V, indicating excellent ORR catalytic activity. This remarkable improvement in activity was attributed to the shift of the *d*-band center of Ni atom towards the Fermi-level while the shift of the *d*-band center of Pd atom away from the Fermi-level after O doping, leading to the transformation of adsorption configuration of *OH from binding with Ni and Pd atoms into only binding Ni atom and thus the decreased adsorption strength to *OH. This work sheds light on development of high-performance graphene-based DACs toward ORR by edge and doping engineering.

Data availability

Data is provided within the manuscript or supplementary information files.

Received: 7 January 2025; Accepted: 4 March 2025
Published online: 14 March 2025

References

1. Chu, S. & Majumdar, A. Opportunities and challenges for a sustainable energy future. *Nature* **488**(7411), 294–303 (2012).
2. Debe, M. K. Electrocatalyst approaches and challenges for automotive fuel cells. *Nature* **486**(7401), 43–51 (2012).
3. Cano, Z. P. et al. Batteries and fuel cells for emerging electric vehicle markets. *Nat. Energy* **3**(4), 279–289 (2018).
4. Wang, H. F. & Xu, Q. Materials design for rechargeable metal-Air batteries. *Matter* **1**(3), 565–595 (2019).
5. Huang, L. et al. Advanced platinum-based oxygen reduction electrocatalysts for fuel cells. *Acc. Chem. Res.* **54**(2), 311–322 (2021).
6. Kodama, K., Nagai, T., Kuwaki, A., Jinnouchi, R. & Morimoto, Y. Challenges in applying highly active Pt-based nanostructured catalysts for oxygen reduction reactions to fuel cell vehicles. *Nat. Nanotechnol.* **16**(2), 140–147 (2021).
7. Ying, Y. R., Luo, X., Qiao, J. L. & Huang, H. T. "More is different:" synergistic effect and structural engineering in double-atom Catalysts. *Adv. Funct. Mater.* **31**(3), 2007423 (2020).
8. Zhang, W. Y. et al. Emerging dual-atomic-site catalysts for efficient energy catalysis. *Adv. Mater.* **33**(36), 2102576 (2021).
9. Pedersen, A. et al. Dual-metal atom electrocatalysts: Theory, synthesis, characterization, and applications. *Adv. Energy Mater.* **12**(3), 2102715 (2021).
10. Li, R. Z. & Wang, D. S. Superiority of dual-atom catalysts in electrocatalysis: One step further than single-atom catalysts. *Adv. Energy Mater.* **12**(9), 2103564 (2022).
11. Shang, H. S. & Liu, D. Atomic design of carbon-based dual-metal site catalysts for energy applications. *Nano Res.* **16**(5), 6477–6506 (2023).
12. Wang, F. T., Xie, W. B., Yang, L. J., Xie, D. Q. & Lin, S. Revealing the importance of kinetics in N-coordinated dual-metal sites catalyzed oxygen reduction reaction. *J. Catal.* **396**, 215–223 (2021).
13. Cui, H. et al. Dynamics of non-metal-regulated FeCo bimetal microenvironment on oxygen reduction reaction activity and intrinsic mechanism. *Nano Res.* **16**(2), 2199–2208 (2023).
14. Karmodak, N. & Nørskov, J. K. Activity and stability of single- and di-atom catalysts for the O_2 reduction reaction. *Angew. Chem. Int. Ed.* **62**(47), e202311113 (2023).
15. Zhang, L. et al. Microenvironment regulation of M-N-C single-atom catalysts towards oxygen reduction reaction. *Nano Res.* **16**(4), 4468–4487 (2023).
16. Fu, X. Z. et al. Atomically dispersed Ni-N_3 sites on highly defective micro-mesoporous carbon for superior CO_2 electroreduction. *Small* **18**(20), 2107997 (2022).
17. Ma, R. G. et al. Edge-sited Fe-N_4 atomic species improve oxygen reduction activity via boosting O_2 dissociation. *Appl. Catal. B Environ.* **265**, 118593 (2020).
18. Chen, G. B. et al. Highly accessible and dense surface single metal FeN_4 active sites for promoting the oxygen reduction reaction. *Energy Environ. Sci.* **15**(6), 2619–2628 (2022).
19. Li, J. J. et al. Metal-organic framework-derived graphene mesh: A robust scaffold for highly exposed Fe-N active sites toward an excellent oxygen reduction catalyst in acid media. *J. Am. Chem. Soc.* **144**(21), 9280–9291 (2022).
20. Saputro, A. G. et al. Formation of tilted FeN_4 configuration as the origin of oxygen reduction reaction activity enhancement on a pyrolyzed Fe-N-C catalyst with FeN_4-edge active sites. *J. Phys. Chem. C* **125**(36), 19682–19696 (2021).
21. Hu, R. M., Li, Y. C., Zeng, Q. W. & Shang, J. X. Role of active sites in N-coordinated Fe-Co dual-metal doped graphene for oxygen reduction and evolution reactions: A theoretical insight. *Appl. Surf. Sci.* **525**, 146588 (2020).
22. Zhao, M. Y., Gan, G. Y. & Zhang, Q. J. Different bonding defects on dual-metal single-atom electrocatalyst $CoZnN_6$(OH) for oxygen reduction reaction. *ChemPhysChem* **23**(8), e202100902 (2022).
23. Jiang, M. et al. Rationalization on high-loading iron and cobalt dual metal single atoms and mechanistic insight into the oxygen reduction reaction. *Nano Energy* **93**, 106793 (2022).
24. Zhong, D. C., Gong, Y. N., Zhang, C. & Lu, T. B. Dinuclear metal synergistic catalysis for energy conversion. *Chem. Soc. Rev.* **52**(9), 3170–3214 (2023).
25. Li, L. et al. Exploring highly efficient dual-metal-site electrocatalysts for oxygen reduction reaction by first principles screening. *J. Electrochem. Soc.* **169**(2), 026524 (2022).
26. Zhu, X. R. et al. Activity origin and design principles for oxygen reduction on dual-metal-site catalysts: A combined density functional theory and machine learning study. *J. Phys. Chem. Lett.* **10**(24), 7760–7766 (2019).
27. Cao, L. J., Shao, Y. F., Pan, H. & Lu, Z. G. Designing efficient dual-metal single-atom electrocatalyst TMZnN6 (TM = Mn, Fe Co, Ni, Cu, Zn) for oxygen reduction reaction. *J. Phys. Chem. C* **124**(21), 11301–11307 (2020).
28. Thi, M. L. N., Tran, T. H., Anh, P. D. H., Nhac-Vu, H. T. & Bui, Q. B. An innovative catalyst of nickel-palladium alloy nanocrystals embedded nitrogen-doped graphene for efficient oxygen reduction reaction. *J. Alloys Compd.* **797**, 314–324 (2019).
29. Balčiūnaitė, A. et al. Effective fuel cell electrocatalyst with ultralow Pd loading on Ni-N-doped graphene from upcycled water bottle waste. *Sustainability* **16**(17), 7469 (2024).
30. Chasanah, U. et al. Effect of stabilizer agent type on the characteristics of Pd–Ni nanoparticles deposited on reduced graphene oxide as electrocatalysts for the oxygen reduction reaction. *J. Mater. Sci.* **59**(44), 20593–20605 (2024).
31. Yin, C., Tang, H., Li, K., Yuan, Y. & Wu, Z. J. Theoretical insight into the catalytic activities of oxygen reduction reaction on transition metal–N_4 doped graphene. *New J. Chem.* **42**(12), 9620–9625 (2018).
32. Li, L., Huang, R., Cao, X. R. & Wen, Y. H. Computational screening of efficient graphene-supported transition metal single atom catalysts toward oxygen reduction reaction. *J. Mater. Chem. A* **8**(37), 19319–19327 (2020).

33. Xue, Z., Zhang, X. Y., Qin, J. Q. & Liu, R. P. TMN_4 complex embedded graphene as bifunctional electrocatalysts for high efficiency OER/ORR. *J. Energy Chem.* **55**, 437–443 (2021).
34. Sun, J. K. et al. Heteroatom doping regulates the catalytic performance of single-atom catalyst supported on graphene for ORR. *Nano Res.* **17**, 1086–1093 (2024).
35. Wang, C. L. et al. Engineering the coordination environment enables molybdenum single-atom catalyst for efficient oxygen reduction reaction. *J. Catal.* **389**, 150–156 (2020).
36. Liu, Y. R. et al. Optimizing Fe-3d electron delocalization by asymmetric Fe–Cu diatomic configurations for efficient anion exchange membrane fuel cells. *Adv. Energy Mater.* **13**(46), 2302719 (2023).
37. Zhang, Y. X. et al. General synthesis of a diatomic catalyst library via a macrocyclic precursor-mediated approach. *J. Am. Chem. Soc.* **145**(8), 4819–4827 (2023).
38. Kresse, G. & Furthmuller, J. Efficient iterative schemes for ab initio total-energy calculations using a plane-wave basis set. *Phys. Rev. B* **54**(16), 11169–11186 (1996).
39. Kresse, G. & Furthmüller, J. Efficiency of ab-initio total energy calculations for metals and semiconductors using a plane-wave basis set. *Comp. Mater. Sci.* **6**(1), 15–50 (1996).
40. Perdew, J. P., Burke, K. & Ernzerhof, M. Generalized gradient approximation made simple. *Phys. Rev. Lett.* **77**(18), 3865–3868 (1996).
41. Grimme, S., Antony, J., Ehrlich, S. & Krieg, H. A consistent and accurate ab initio parametrization of density functional dispersion correction (DFT-D) for the 94 elements H-Pu. *J. Chem. Phys.* **132**, 154104 (2010).
42. Sun, Y. L. et al. Itinerant ferromagnetic half metallic cobalt–iron couples: Promising bifunctional electrocatalysts for ORR and OER. *J. Mater. Chem. A* **7**(47), 27175–27185 (2019).
43. Liang, Z. et al. Evaluating the catalytic activity of transition metal dimers for the oxygen reduction reaction. *J. Colloid Interf. Sci.* **568**, 54–62 (2020).
44. Li, L., Li, Y. M., Huang, R., Cao, X. R. & Wen, Y. H. Boosting the electrocatalytic activity of Fe–Co dual-atom catalysts for oxygen reduction reaction by ligand-modification engineering. *ChemCatChem* **13**(21), 4645–4651 (2021).
45. Huang, K. W. et al. NiPd co-doped nitrogen-coordinated graphene as a high-efficiency electrocatalyst for oxygen reduction reactions: A first-principles determination. *Phys. Chem. Chem. Phys.* **25**(27), 18266–18274 (2023).
46. Li, L., Wu, X. X., Du, Q. Y., Bai, N. & Wen, Y. H. Boosting the oxygen reduction reaction activity of dual-atom catalysts on N-doped graphene by regulating the N coordination environment. *Phys. Chem. Chem. Phys.* **26**(1), 628–634 (2024).
47. Tripkovic, V., Skúlason, E., Siahrostami, S., Norskov, J. K. & Rossmeisl, J. The oxygen reduction reaction mechanism on Pt(111) from density functional theory calculations. *Electrochim. Acta* **55**(27), 7975–7981 (2010).
48. Duan, Z. Y. & Wang, G. F. Comparison of reaction energetics for oxygen reduction reactions on Pt(100), Pt(111), Pt/Ni(100), and Pt/Ni(111) surfaces: A first-principles study. *J. Phys. Chem. C* **117**(12), 6284–6292 (2013).
49. Mathew, K., Sundararaman, R., Letchworth-Weaver, K., Arias, T. A. & Hennig, R. G. Implicit solvation model for density-functional study of nanocrystal surfaces and reaction pathways. *J. Chem. Phys.* **140**(8), 084106 (2014).

Acknowledgements

This work was financially supported by the Natural Science Foundation of Inner Mongolia Autonomous Region (Grant Nos. 2023QN01010 and 2024MS01004), the Research Program of Science and Technology at Universities of Inner Mongolia Autonomous Region (Grant No. NJZZ23019), and the Fundamental Research Funds for the Inner Mongolia Normal University (Grant No. 2023JBYJ016), and the Funds for Reform and Development of Local Universities Supported by The Central Government (Cultivation of First-Class Disciplines in Physics).

Author contributions

Lei Li: Data curation, Formal analysis, Investigation, Methodology, Writing-original draft. Xiaoxia Wu: Investigation, Data curation, Formal analysis. Ruotong Zhang: Data curation, Methodology. Narsu Bai: Formal analysis, Supervision. Min Zhang: Conceptualization, Validation. Yuhua Wen: Conceptualization, Supervision, Validation, Writing-review & editing.

Declarations

Competing interests

The authors declare no competing interests.

Additional information

Supplementary Information The online version contains supplementary material available at https://doi.org/10.1038/s41598-025-93115-0.

Correspondence and requests for materials should be addressed to L.L. or Y.W.